Microwave spectroscopy and Zeeman effect of cesium $(n + 2)D_{5/2} \rightarrow nF_J$ Rydberg transitions

Jingxu Bai,[1] Rong Song,[1] Zhenhua Li,[1] Yuechun Jiao [⦾],[1,2,*] Georg Raithel [⦾],[3] Jianming Zhao [⦾],[1,2,†] and Suotang Jia[1,2]

[1]*State Key Laboratory of Quantum Optics and Quantum Optics Devices, Institute of Laser Spectroscopy,*
Shanxi University, Taiyuan 030006, People's Republic of China
[2]*Collaborative Innovation Center of Extreme Optics, Shanxi University, Taiyuan 030006, People's Republic of China*
[3]*Department of Physics, University of Michigan, Ann Arbor, Michigan 48109-1120, USA*

We report on high-resolution microwave spectroscopy of cesium Rydberg $(n + 2)D_{5/2} \rightarrow nF_J$ transitions in a cold atomic gas. Atoms laser-cooled and trapped in a magnetic-optical trap are prepared in the D Rydberg state using a two-step laser excitation scheme. A microwave field transmitted into the chamber with a microwave horn drives the Rydberg transitions, which are probed via state selective field ionization. Varying duration and power of the microwave pulse, we observe Fourier sideband spectra as well as damped, on-resonant Rabi oscillations with pulse areas up to $\gtrsim 3\pi$. Furthermore, we investigate the Zeeman effect of the clearly resolved nF_J fine-structure levels in fields up to 120 mG, where the transition into $nF_{7/2}$ displays a thee-peak Zeeman pattern, while $nF_{5/2}$ shows a two-peak pattern. Our theoretical models explain all observed spectral characteristics, showing good agreement with the experiment. Our measurements provide a pathway for the study of high-angular-momentum Rydberg states, initialization and coherent manipulation of such states, Rydberg-atom macrodimers, and other Rydberg-atom interactions. Furthermore, the presented methods are suitable for calibration of microwave radiation as well as for nulling and calibration of dc magnetic fields in experimental chambers for cold atoms.

I. INTRODUCTION

Rydberg atoms with principal quantum numbers $n \gtrsim 10$ have exaggerated properties [1], such as long lifetimes ($\sim n^3$), large microwave electric-dipole transition matrix elements ($\sim n^2$), enormous electric polarizabilities ($\sim n^7$), and strong van der Waals ($\sim n^{11}$) and other Rydberg-atom interactions [2,3]. These properties are the foundation for recent developments in single-atom manipulation [2,4], single-photon sources [5–8], quantum information and simulation [9–11], as well as precise quantum measurements [12–17]. The coupling of nuclear, $\mathbf{I}$, and electronic angular momenta, $\mathbf{J} = \mathbf{L} + \mathbf{S}$, causes hyperfine and fine structure splittings and shifts [18,19] [$\mathbf{L}$ and $\mathbf{S}$ denote orbital and spin angular momentum of the electron(s)]. The high sensitivity of Rydberg atoms to microwave fields, combined with their Zeeman and Paschen-Back effects, leads to rich spectroscopic structures. In room temperature cells, Zhang *et al.* [20,21] have observed the Zeeman effect of Cs Rydberg atoms in a magnetic field. Cheng *et al.* [22] have conducted high-precision spectroscopy of Rydberg-level splittings in an external magnetic field with two different optical polarization combinations of $\sigma^+ \pm \sigma^-$ for probe and coupling laser beams in ladder-type electromagnetically induced transparency (EIT). In a cesium cold-atom experiment with a controllable magnetic field, Xue *et al.* [23] have investigated the influence of Zeeman splittings, optical

pumping, and probe-light-induced radiation pressure in cold-atom Rydberg-EIT spectra. Recently, laser frequencies could be stabilized to Rydberg transitions using Zeeman-modulation Rydberg-EIT spectroscopy [24,25]. This method is applicable to a variety of applications in modern-physics research, including quantum information processing [10,11], many-body dynamics [26], and Rydberg molecules [27].

Microwave spectroscopy of Rydberg atoms, which typically has a resolution limit in the range of about 10 kHz, is well suited to measure energy levels and quantum defects of Rydberg states for which no convenient laser excitation schemes exist, such as high-ℓ ($\ell = 3$, 4, and 5) states of rubidium [28–31] and cesium [32–34]. Recently, Cardman *et al.* [35] have measured the hyperfine structure (HFS) and Zeeman effect of $nP_{1/2}$ Rydberg states using narrow-linewidth millimeter-wave spectroscopy in a cold ^{85}Rb ensemble.

In the present work, we report on high-resolution microwave spectroscopy of $(n + 2)D_{5/2} \rightarrow nF_J$ transitions by scanning a weak microwave field in a cold Cs Rydberg atom sample. In our first study we change the microwave pulse duration and power at zero magnetic field to establish the spectral resolution. We observe symmetric, high-contrast Fourier-sideband spectra that demonstrate coherent excitation for microwave pulses of up to several microseconds in duration, while at 20 μs we reach our linewidth limit of ~ 140 kHz. The fine structure (FS) splitting of the nF_J levels is clearly resolved in all cases. In the second part of our work, we apply a controlled homogeneous magnetic field using a pair of Helmholtz coils, and perform high-precision Zeeman spectroscopy for both FS components $nF_{5/2}$ and

---

*ycjiao@sxu.edu.cn
†zhaojm@sxu.edu.cn
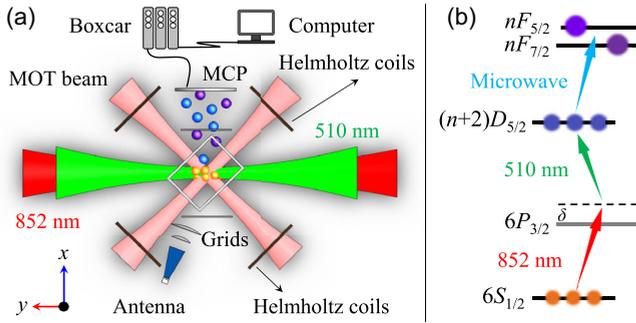
FIG. 1. (a) Schematic of the experimental setup. Cesium atoms are cooled and trapped at the center of a MOT. Two excitation lasers (wavelengths 852 nm and 510 nm) are overlapped and counterpropagated through the MOT to prepare $(n+2)D_{5/2}$ Rydberg atoms. A tunable microwave field, applied via a microwave horn, allows us to perform high-resolution spectroscopy of $(n+2)D_{5/2} \rightarrow nF_J$ transitions. Three pairs of orthogonal electric grids and Helmholtz coils are employed to compensate stray electric and magnetic fields, respectively, and to scan the magnetic field in the z direction for Zeeman-effect studies. Rydberg-atom electric-field ionization and time-resolved ion detection allow us to measure Rydberg-transition probabilities. See text for details. (b) Energy level diagram. The 852-nm and 510-nm lasers populate the $(n+2)D_{5/2}$ Rydberg state via a two-step excitation process, which is off-resonant from the intermediate $6P_{3/2}$ state by $\delta/2\pi = 330$ MHz. The tunable microwave field drives $(n+2)D_{5/2}$ to nF_J transitions.

$nF_{7/2}$. We observe two-peak and three-peak Zeeman splitting patterns, respectively, in agreement with calculations. The high-resolution Zeeman spectroscopy of high-angular-momentum ($\ell = 3$) Rydberg states, presented in our work, will be helpful for *in situ* calibration of magnetic fields in cold-atom and cold-molecule research, it may enhance the accuracy of future studies of high-ℓ quantum defects, and it may serve well in future quantum-control and -simulation studies involving high-ℓ Rydberg states.

II. EXPERIMENTAL SETUP

The experimental setup is shown in Fig. 1(a). Cesium atoms are cooled and trapped in a magneto-optical trap (MOT) with a density of $\sim 10^{10}$ cm^{-3} and a temperature of $\sim 100 \, \mu$K. The MOT magnetic field and the MOT laser beams are switched off 3 ms and 1 ms before application of the 852-nm and 510-nm Rydberg-excitation laser pulses. The laser pulses are coincident, have a duration of $t = 1 \, \mu$s, and have respective Gaussian beam-waist parameters of $\omega_{852} = 750 \, \mu$m and $\omega_{510} = 1000 \, \mu$m, with $\omega_{852(510)}$ denoting the radii at which the respective intensities are reduced by a factor of $1/e^2$ from their peak values. Also, the two lasers are counterpropagated along the y axis and have parallel linear polarizations along the x axis. The effective Rabi frequency of the two-step Rydberg excitation is kept at $\Omega_{2Ph} = \Omega_{852}\Omega_{510}/(2\delta) \approx 2\pi \times 9$ kHz, where Ω_{852} and Ω_{510} denote the one-step Rabi frequencies at the beam centers, resulting in a Rydberg-atom excitation probability of $(\Omega_{2Ph} t)^2/4 \approx 0.8 \times 10^{-3}$. At our MOT atom density, this is sufficiently low that Rydberg-atom interactions remain at a tolerable level in our experiment. The microwave field ranges in frequency from 22 GHz to 33 GHz and is

emitted by a small antenna into the chamber. Since the chamber is largely made from metal, the calibration factor between microwave field strength and square root of power must be determined experimentally based upon the measured atomic response (see Sec. III A).

Three pairs of electric grids with symmetry points centered at the MOT are placed on the x, y, and z axes (in Fig. 1 we only show the pair of grids on the x axis). The grids are used to compensate stray electric fields and to apply an electric-field ramp for state-selective electric-field ionization and detection of the Rydberg atoms. After electric-field compensation, quadratic dc Stark shifts (and therefore Stark-effect-induced line-broadening effects) of the microwave transitions are within a few kHz (see Ref. [34], where our setup is described in detail). The liberated ions are accelerated to reach the microchannel plate (MCP) detector. Time-resolved ion signals, recorded with a boxcar integrator and processed on a computer, yield the Rydberg-state populations. Furthermore, three orthogonal pairs of Helmholtz coils are placed around the chamber to compensate stray magnetic fields and to apply controlled magnetic fields to investigate the Zeeman splitting of the $(n+2)D_{5/2}$ to nF_J microwave transitions. The stray magnetic field is less than 5 mG after compensation. The resultant Zeeman broadening is limited to about 10 kHz and is approximately symmetric [34].

Figure 1(b) shows the level diagram. The $(n+2)D_{5/2}$ state is populated via two-step laser excitation from $6S_{1/2}$ into $(n+2)D_{5/2}$. The two-step transition is blue-detuned from the intermediate $6P_{3/2}$ state by $\delta/2\pi = 330$ MHz in order to reduce photon scattering and light radiation pressure. In the experiment, the 852-nm laser is locked with modulation-free polarization spectroscopy [36], and the 510-nm laser is locked to a Fabry-Perot cavity with a finesse of 1.5×10^4 using the Pound-Drever-Hall technique [37]. The linewidths of both locked lasers are less than 100 kHz. The frequency of the microwave field, which is radiated into the chamber from a microwave horn, is scanned across selected $(n+2)D_{5/2}$ to nF_J transitions to obtain narrow-linewidth Rydberg microwave spectra.

III. RESULTS AND DISCUSSION

A. Fourier sideband spectroscopy

In our first experiment, the frequency of the 510-nm laser is tuned to excite the $48D_{5/2}$ state. Electric and magnetic fields are set to zero, within the uncertainties of the field compensation routine. The microwave field then drives the transition $48D_{5/2} \rightarrow 46F_{7/2}$. Microwave spectra are obtained by state-selective field ionization and gated ion detection, as the microwave frequency is scanned across the $48D_{5/2} \rightarrow 46F_{7/2}$ transition (center frequency 29.74323 GHz and scan ranges from 1.6 MHz to 8 MHz). In Fig. 2(a), we present a typical microwave spectrum of the transition for a microwave square pulse with duration $\tau = 1 \, \mu$s. The spectrum in Fig. 2(a) has a FWHM linewidth of 705 kHz. For nonsaturated excitation by an ideal square pulse of duration $\tau = 1 \, \mu$s, the spectrum $S(\Delta)$ would follow $S(\Delta) \propto |\text{sinc}(\tau \Delta/2)|^2$, which would have a FWHM of $0.89/\tau \approx 890$ kHz. The experimental width is slightly less, possibly due to a deviation of the exact rf pulse shape from a perfect square pulse.
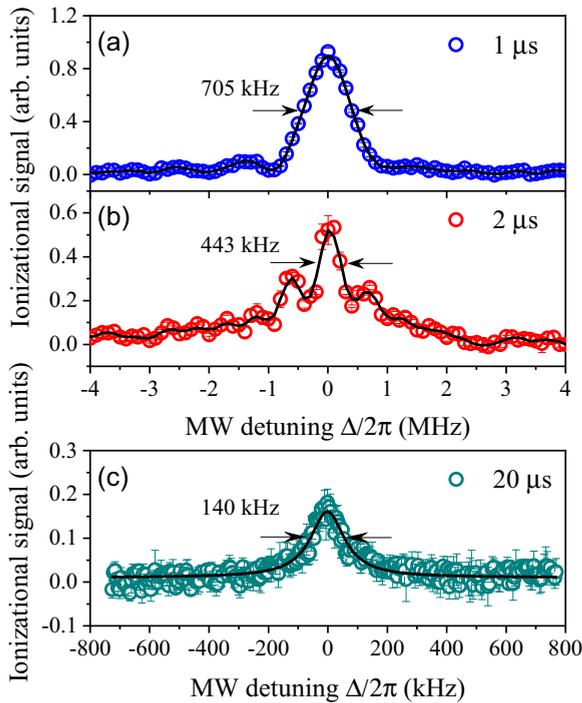
FIG. 2. Measurements of microwave spectra of the $48D_{5/2} \to 46F_{7/2}$ transition with the power of the signal generator set to -50 dBm, a scan step size 100 kHz, and pulse durations of (a) 1 μs and (b) 2 μs. Black lines show smoothed curves obtained with the Savitzky-Golay method. We clearly observe Fourier sidebands. The spectrum in (a) is below saturation, while the one in (b) is somewhat saturated (for details see text). (c) Spectrum at -72 dBm, scan step size 5 kHz, and pulse duration $\tau = 20$ μs. The Lorentzian fit (black curve) has a full width at half maximum (FWHM) of 140 kHz. Error bars show the standard error of the mean (SEM) of the samples. The stated microwave powers reflect the signal-generator settings. (The electric fields experienced by the atoms are calibrated against signal-generator power near the end of Sec. III A.)

In order to reduce the linewidth, in Figs. 2(b) and 2(c) we increase the microwave pulse duration τ to 2 μs and 20 μs, respectively. The width of the central lobe in Fig. 2(b) agrees well with the (unsaturated) Fourier limit of 445 kHz; however, the overall width of the spectrum, including its side lobes, is considerably wider due to the onset of saturation. The experimental linewidth limit of 140 kHz is reached in Fig. 2(c), where we have reduced the microwave Rabi frequency by about a factor of 12.5 and increased τ by a factor of 10 relative to Fig. 2(b). The FWHM width in Fig. 2(c) is about three times larger than the Fourier limit (which is 45 kHz for a $\tau = 20$ μs pulse). The excess width is mostly attributed to Zeeman shifts of the different magnetic sublevels in the residual stray magnetic field, as well as to resonant dipolar Rydberg-atom interactions. The dipolar interactions of $(n + 2)D_{5/2}\text{-}nF_J$ pair states scale as $C_3 R^{-3}$ with dispersion coefficients $|C_3/h| \sim n^4 \times 0.5 \, \text{kHz} \, \mu\text{m}^3$ and $|C_3/h| \sim n^4 \times 0.03 \, \text{kHz} \, \mu\text{m}^3$ for $J = 7/2$ and $5/2$, respectively [34]. For $n = 46$ and our Rydberg atom density $\sim 4 \times 10^6$ cm^{-3}, which corresponds to a nearest-neighbor distance of $R \approx 35$ μm, the respective dipolar frequency shifts are on the order of 50 kHz and 3.2 kHz. These interaction shifts are approximately symmetric about

the line centers [34] and are large enough to be a leading source of our experimentally observed linewidth limit. We also note that the Rydberg–van der Waals shifts are orders of magnitudes smaller than the resonant dipolar shifts [34].

Next we comment on the Fourier-sideband strengths. In the case of weak saturation, where the microwave Rabi frequency $\Omega < |\Delta|$ on the Fourier sidebands, the amplitude of the sidebands rapidly diminishes with order (the first sidebands have a strength of 4.7% of the central peak, the second sidebands have 1.6%, etc.). Figure 2(a) is near the weak-saturation limit. With increasing saturation, where $|\Delta| \lesssim \Omega$ within at least the first sideband, the sidebands rise in strength relative to the central peak, as is evident in Fig. 2(b).

In order to exhibit the spectral dependence on both microwave power and Δ, as well as to estimate the degree of coherence in the excitation process, in Fig. 3 we show a series of measured microwave spectra for microwave powers in the range between -35 dBm and -62.5 dBm and over a detuning range $|\Delta| \lesssim 2\pi \times 15$ MHz, for fixed $\tau = 1$ μs. In Figs. 3(a)–3(d), we present selected microwave spectra of $48D_{5/2} \to 46F_J$ for microwave powers as indicated. Gray vertical dashed lines mark the resonant transition frequencies of 29.743 GHz and 29.753 GHz for $46F_{7/2}$ and $46F_{5/2}$, respectively. Due to the interaction between the atomic core and the valence electron, the FS of the Rydberg F-state is inverted, resulting in a greater transition frequency for $46F_{5/2}$ than for $46F_{7/2}$. Also, since angular transition matrix elements for $46F_{7/2}$ are much greater than those for $46F_{5/2}$, the peak intensity of the $46F_{7/2}$ exceeds that of the $46F_{5/2}$ signal. The $46F_{7/2}$ line also is considerably more susceptible to broadening due to dipole-dipole interactions than the $46F_{5/2}$ line [34].

While the radial transition matrix elements for the $48D_{5/2} \to 46F_{7/2}$ and the $48D_{5/2} \to 46F_{5/2}$ transitions are nearly identical, the squares of the angular matrix elements averaged over magnetic quantum numbers differ by a factor of 20, equivalent to 13 dB in microwave power. As a result, the onset of the $F_{5/2}$ line in Fig. 3 is shifted to higher power relative to that of the $F_{7/2}$ line. The $48D_{5/2} \to 46F_{5/2}$ transition remains unsaturated throughout the investigated power range and only becomes visible at powers above -47.5 dBm, while the $48D_{5/2} \to 46F_{7/2}$ transition becomes saturated. Due to its larger Rabi frequency, the $46F_{7/2}$ line develops visible Fourier side bands at powers above about -50 dBm and becomes saturation broadened [see Figs. 3(a)–3(e2)]. In their respective unsaturated regimes, both lines have a FWHM of about 800 kHz, which is at the Fourier limit for $\tau = 1$ μs.

The cuts through the spectrum shown in Figs. 3(a)–3(d) correspond with approximate resonant pulse areas of $\pi/2$, π, 2π, and 3π for the $48D_{5/2} \to 46F_{7/2}$ transition, averaged over m_J. At the resonant frequency of the $48D_{5/2} \to 46F_{7/2}$ transition we observe a damped Rabi oscillation, as is evident in Fig. 3(f).

In our model for the spectra in Figs. 2–4 the optical $6S_{1/2}$ to $(n + 2)D_{5/2}$ transitions between the various magnetic sublevels are modeled as two-step transitions that are far-off-resonant from the intermediate $6P_{3/2}$ state, with both optical fields polarized along x, and with the HFS of all levels included. The optical two-step transition matrix elements between coupled pairs of $|6S_{1/2}, F = 4, m_F\rangle$ and $|(n + 2)D_{5/2}, F'', m_{F''}\rangle$ states are coherent sums
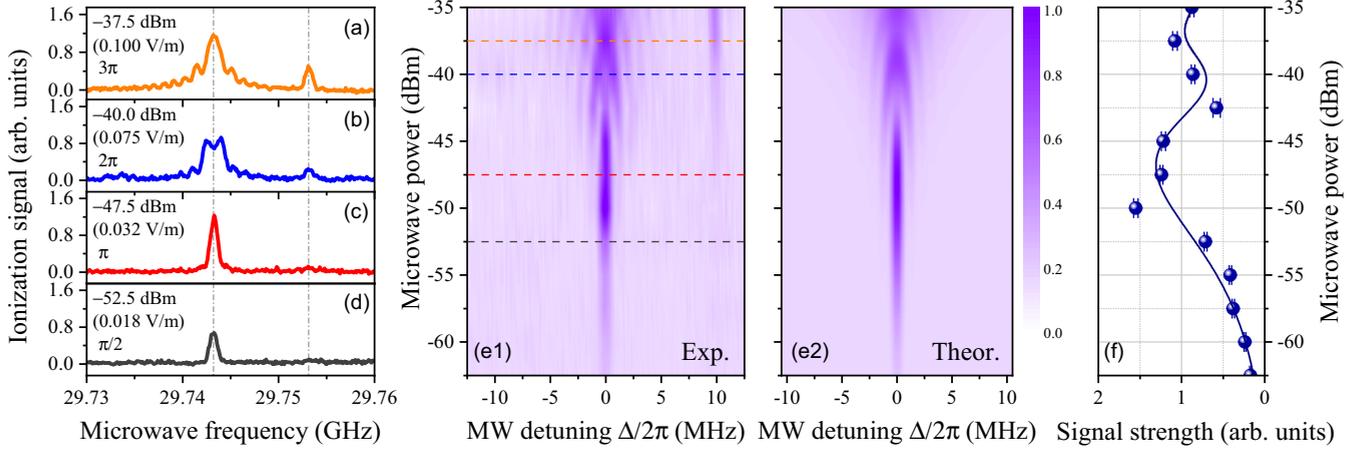
FIG. 3. Measurements of microwave spectra of $48D_{5/2} \rightarrow 46F_J$ transition as a function of microwave frequency for the indicated microwave powers of the signal generator in dBm. (Electric fields at the location of the atoms are calibrated against signal-generator power near the end of Sec. III A.) The two vertical gray dash-dotted lines in (a)–(d) at 29.743 GHz and 29.753 GHz mark the resonant frequencies for $46F_{7/2}$ (left) and $46F_{5/2}$ (right), respectively. The indicated pulse areas Φ are estimates for resonant excitation of $46F_{7/2}$ with our 1-μs microwave pulse. Each spectrum is an average over 20 measurements. (e1) Contour plot of microwave spectra as a function of microwave detuning Δ and for the power ranging from -62.5 dBm to -35 dBm in steps of 2.5 dB. The four horizontal dashed lines mark the spectra of (a) (orange), (b) (blue), (c) (red) and (d) (gray), respectively. (e2) Simulation result for (e1), only showing the signal of $46F_{7/2}$. (f) Measured signal strength of the resonant transition $48D_{5/2} \rightarrow 46F_{7/2}$ as a function of microwave power, showing a damped Rabi oscillation, and fit (see text).
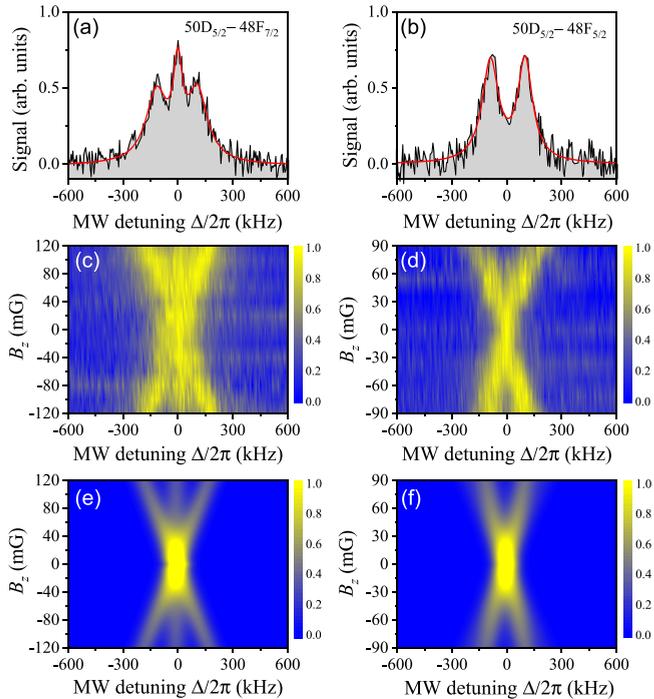
FIG. 4. Measurements and simulations of Zeeman spectra of the $50D_{5/2} \rightarrow 48F_J$ microwave transitions. (a and b) Zeeman spectra for $J = 7/2$ at $B = 83$ mG and for $J = 5/2$ at 58 mG, respectively. Red curves display the results of multipeak Lorentzian fits. Normalized color-scale plots of measured Zeeman spectra, taken over a range of B, are shown in (c) and (d) for $J = 7/2$ and $J = 5/2$, respectively. (e and f) Results of corresponding simulations, in which the angle between the polarizations of the microwave and magnetic fields is set to 55°, which leads to good agreement between experiment and simulations.

over the intermediate-state manifold, $|6P_{3/2}, F', m_{F'}\rangle$, with intermediate-state detunings that depend on δ from Fig. 1, the HFS quantum numbers F, m_F, F', and $m_{F'}$ of the $6S_{1/2}$ and $6P_{3/2}$ states, respectively, and the optional magnetic field, which points along z. In the computation the z axis is used as the quantization axis. The two-step optical transition probabilities between the $6S_{1/2}$ and $(n + 2)D_{5/2}$ HFS sublevels further depend on the two-step detunings, which generally depend on m_F, F'', and $m_{F''}$ via the HFS and the Zeeman effect. For our $t = 1$-μs optical pulses and the magnetic-field range of interest, the dependencies of the two-step transition probabilities on m_F and $m_{F''}$ via the Zeeman effect are insignificant, as is the splitting between the HFS states of the $(n + 2)D_{5/2}$ Rydberg level, F''. Under the reasonable assumption that the initial $6S_{1/2}$ atom sample is not magnetized, we obtain the population distribution over the $|(n + 2)D_{5/2}, F'', m_{F''}\rangle$ states by taking incoherent sums over the squares of all two-step matrix elements between $|6S_{1/2}, F = 4, m_F\rangle$ and $|(n + 2)D_{5/2}, F'', m_{F''}\rangle$, with summing index m_F. The probabilities $P(F'', m_{F''})$ of the $|(n + 2)D_{5/2}, F'', m_{F''}\rangle$ are then used to model the $(n + 2)D_{5/2} \rightarrow nF_J$ microwave spectra for $J = 5/2$ or $7/2$. The microwave field is assumed to be linearly polarized in the xz plane with a polar polarization angle of θ_{MW} with respect to the z axis. While the azimuthal angle of the microwave polarization ϕ_{MW} can be varied in the simulation, we have verified that it is insignificant due to the absence of Zeeman coherences in the $(n + 2)D_{5/2}$ level. The spectra are summed over all $|(n + 2)D_{5/2}, F'', m_{F''}\rangle$ using the $P(F'', m_{F''})$ as weights, yielding model spectra $S(\Delta)$ versus the microwave detuning Δ.

The HFS splittings of our $(n + 2)D_{5/2}$ Rydberg levels are only in the 10-kHz range and are therefore marginally significant, and those of the $(n + 2)F_J$ levels are even smaller

(and unknown to us). For more transparency, the probability distributions $P(F'', m_{F''})$ that result from the optical two-step excitation may therefore be traced over the nuclear quantum numbers, leading to reduced distributions $\tilde{P}(m_J)$ that only

depend on the electronic m_J quantum number of the $(n+2)D_{5/2}$ level. With the Rydberg HFS removed, the $\tilde{P}(m_J)$ lead to simplified expressions for the model spectra $S(\Delta)$. For instance, for $\theta_{\mathrm{MW}} = 0$ the model spectra can be written as

$$S(\Delta) = \sum_{m_J} A \, \tilde{P}(m_J) \frac{\Omega_{m_J}^2}{\Delta^2 + \Omega_{m_J}^2} \Big[1 - \exp\Big(-\tau\,\gamma\,\sqrt{\Delta^2 + \Omega_{m_J}^2} \Big) \cos\Big(\tau\,\sqrt{\Delta^2 + \Omega_{m_J}^2} \Big) \Big], \qquad (1)$$

where $\Delta/(2\pi)$ is the microwave detuning in Hz, A is an amplitude fit parameter, $\tilde{P}(m_J)$ are the probabilities for the m_J sublevels of $(n+2)D_{5/2}$ obtained as explained above, $\Omega_{m_J}/(2\pi)$ are the m_J-dependent microwave Rabi frequencies in Hz, and γ is a damping parameter. The microwave Rabi frequencies in Eq. (1) are

$$\Omega_{m_J} = \frac{e a_0 R_{(n+2)D_{5/2}}^{nF_J} w_{D_{5/2}, m_J}^{F_J, m_J} E_{\mathrm{MW}}}{\hbar}. \qquad (2)$$

Here, R is the radial matrix element, which equals 2564 in atomic units for both J values for $n = 46$, w is the angular matrix element, and E_{MW} is the microwave electric field. The w for $F_{7/2}$ are 0.3499, 0.4518, and 0.4949 for $|m_J| = 5/2, 3/2$, and $1/2$, respectively.

We have modeled the spectra in Fig. 3(e) as Δ- and power-dependent Rabi oscillations according to Eqs. (1) and (2). The exponential damping term has a form $\propto \exp(-\Phi\gamma)$, where $\Phi = \tau\sqrt{\Omega_{m_J}^2 + \Delta^2}$ is the pulse area in rad. Good agreement is found for a damping constant $\gamma \approx 0.088\,\mathrm{rad}^{-1}$, i.e., we are able to observe several Rabi cycles. The visibility reduction of the Rabi oscillation observed for $\Phi \gtrsim 2\pi$ is in part due to the 40% variation of the Rabi frequencies Ω_{m_J} as a function of m_J. The m_J inhomogeneity could be addressed by optical pumping of the sample and by optimizing the optical and microwave polarizations. The level of coherence in Fig. 3 would suffice for applications in quantum control and quantum simulations using ensembles of $\ell = 2$ and $\ell = 3$ Rydberg atoms.

A comparison of measured and simulated spectral maps in Fig. 3(e) allows us to calibrate the microwave electric field at 29.743 GHz. Averaging our calibrations performed for the three pulse areas π, 2π, and 3π, we find $E_{\mathrm{MW}} = 10^{P_{\mathrm{MW}}/20} \times 7.5\,\mathrm{V/m} \pm 12\%$, where P_{MW} is the microwave power at the signal generator in dBm. The uncertainty reflects statistical experimental noise and the power step size of 2.5 dB. By considering relative shifts between the plots in Figs. 3(e1) and 3(e2) along the power axis, and by estimation of the powers at the maxima and minima in Fig. 3(f), we estimate the power calibration uncertainty to be less than ± 1.0 dB. This corresponds with a field calibration uncertainty of less than $\pm 12\%$.

Our simulation for the $46F_{7/2}$ spectrum, plotted for this calibration in Fig. 3(e2), agrees well with the measurement, lending credence to the calibration. Similar calibrations can be performed for other transitions. It is noted that the calibration generally depends on the microwave frequency, because the microwave mode pattern inside the metal vacuum chamber must be assumed to have a complex frequency dependence. However, the calibration is assumed to be constant over the

relatively short frequency ranges used for each set of $(n+2)D_{5/2} \rightarrow nF_J$ transitions. The calibration could be improved by using a smaller power step size by reducing the statistical uncertainty via taking more data for each power setting, and by limiting the data series to the most relevant cut along the line $\Delta = 0$. An improved calibration is, however, not needed for our present purpose. It is further noted that the simulation in Fig. 3(e2) only includes $46F_{7/2}$, while $46F_{5/2}$ is omitted. This is allowable because the $46F_{7/2}$ and $46F_{5/2}$ signals are additive due to the absence of FS mixing in the Hamiltonian, and because the signals are separated well enough to avoid signal overlap between the nF_J components. This remains true even after adding a magnetic field that is too weak to bring the system near the Paschen-Back regime of the FS (as in the next section). Hence, the two nF_J levels are not coupled, and we are allowed to treat them entirely independently.

B. Zeeman spectroscopy

In order to obtain narrow-linewidth microwave spectra in a weak magnetic field, we employ a microwave pulse duration $\tau = 20\,\mu s$ in the Zeeman-splitting measurements presented in this section. After compensation of electric and magnetic stray fields, we apply a small current in the Helmholtz coils on the z axis to generate an uniform magnetic field at the MOT center, which allows us to observe the Zeeman splitting of the $50D_{5/2} \rightarrow 48F_J$ transitions.

Figures 4(a) and 4(b) show Zeeman spectra for microwave fields driving the $50D_{5/2} \rightarrow 48F_{7/2}$ and $50D_{5/2} \rightarrow 48F_{5/2}$ transitions at magnetic fields of 83 and 58 mG, respectively. It is seen that the microwave spectra for $48F_{7/2}$ and $48F_{5/2}$ display different line profiles, namely, three Zeeman peaks for $48F_{7/2}$ and two for $48F_{5/2}$. In the color-scale plots in Figs. 4(c) and 4(d) we present a wider set of measurements for z magnetic fields covering ranges of ± 120 mG and ± 90 mG for $48F_{7/2}$ and $48F_{5/2}$, respectively. It is confirmed that at fields exceeding several tens of mG the $48F_{7/2}$ and $48F_{5/2}$ spectra smoothly split into three and two lines, respectively.

C. Theoretical analysis of Zeeman spectra

To understand the measured Zeeman spectra and the difference between the line profiles for the $nF_{7/2}$ and $nF_{5/2}$ upper states, we first plot all microwave-coupled Zeeman levels in Fig. 5(a) and calculate Zeeman shifts and transition matrix elements for all m_J levels [ignoring the weak Rydberg HFS of the $(n+2)D_{5/2}$ lower state]. In a weak magnetic field, the $(n+2)D_{5/2}$ and nF_J states are in the Zeeman regime of the FS, and the Zeeman shifts exhibit a linear dependence on the magnetic field. The weak magnetic field lifts the
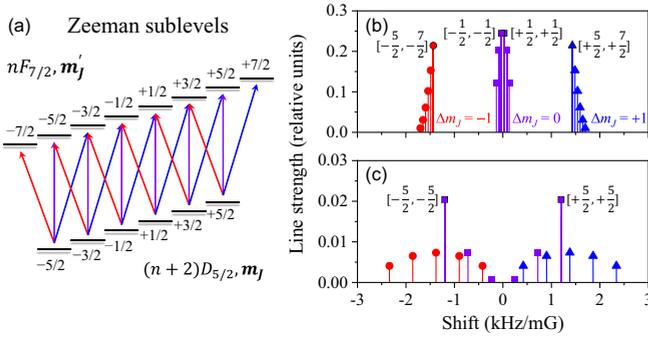
FIG. 5. (a) Zeeman sublevels for the $(n + 2)D_{5/2} \rightarrow nF_{7/2}$ transition in the presence of a weak magnetic field (main separation not to scale). Red, purple, and blue arrows represent the transitions $\Delta m_J = -1$ (σ^-), $\Delta m_J = 0$ (π), and $\Delta m_J = +1$ (σ^+), respectively. The anomalous Zeeman effect for $(n + 2)D_{5/2} \rightarrow nF_{7/2}$ and $(n + 2)D_{5/2} \rightarrow nF_{5/2}$ produces the line patters shown in (b) and (c), respectively. For the line strengths we have assumed x- or z-polarized microwave electric fields; the former drives the $\sigma^{\pm 1}$ transitions with equal strengths, while the latter drives the π transitions. For the $(n + 2)D_{5/2} \rightarrow nF_{7/2}$ transition, the six transition shifts for each $\Delta m_J = 0, \pm 1$ are tightly grouped and well separated, forming a three-peak Zeeman spectrum for cases of mixed microwave polarization. For the $(n + 2)D_{5/2} \rightarrow nF_{5/2}$ transition, the six $\Delta m_J = 0$ lines blend with the five-each $\Delta m_J = -1$ and $\Delta m_J = +1$ lines, generally forming a two-peak Zeeman spectrum, regardless of microwave polarization. The labels $[m_J, m_J']$ mark the transitions with the largest transition probabilities.

degeneracy of the m_J sublevels, as shown in Fig. 5(a). According to electric-dipole selection rules, there are three transition types for changes in m_J, namely, $\Delta m_J = -1, 0, +1$, corresponding to σ^-, π, and σ^+ microwave polarizations. In Fig. 5(a), these are marked with red, purple, and blue arrows, respectively.

Since in our work the magnetic field is in the Paschen-Back regime of the Rydberg HFS and the linear Zeeman regime of the FS, the level shifts from the field-free positions, visualized in Fig. 5(a), are

$$\hbar\Delta_{m_J} = \mu_B B(g_J m_J + g_I m_I), \tag{3}$$

where μ_B is the Bohr magneton, g_J and g_I are the applicable electronic and nuclear g factors, and m_J and m_I the corresponding magnetic quantum numbers. For our $(n + 2)D_{5/2}$ and nF_J Rydberg states of cesium the nuclear term is negligible. The Landé g factors for the electronic Zeeman shifts of the relevant states,

$$g_J \simeq 1 + \frac{J(J + 1) + S(S + 1) - \ell(\ell + 1)}{2J(J + 1)}, \tag{4}$$

are $g_{D_{5/2}} = 1.2$, $g_{F_{7/2}} = 1.1433$, and $g_{F_{5/2}} = 0.8572$. The transition shifts for $\Delta m_J = -1, 0, +1$ can then be expressed as

$$\hbar\Delta(\sigma^-) = \mu_B B \left[m_J (g_{F_J} - g_{D_{5/2}}) - g_{F_J} \right]$$

$$\hbar\Delta(\pi) = \mu_B B \, m_J (g_{F_J} - g_{D_{5/2}})$$

$$\hbar\Delta(\sigma^+) = \mu_B B \left[m_J (g_{F_J} - g_{D_{5/2}}) + g_{F_J} \right]. \tag{5}$$

In Fig. 5(a) we plot the level scheme, and in Figs. 5(b) and 5(c) the relative transition strengths, $|w_{D_{5/2}, m_J}^{F_J, m_J'}|^2$, versus

the line positions from Eq. (5). As seen in Fig. 5(a), for $(n + 2)D_{5/2} \rightarrow nF_{7/2}$ there are six transitions for every Δm_J. Due to the small difference of 0.07 between the lower- and upper-state g_J factors, transitions with the same Δm_J cluster into tight groups, as is evident from Eq. (5) and seen in Fig. 5(b). For mixed microwave polarization, this leads to three peaks in the microwave spectra, in agreement with Figs. 4(a) and 4(c). Residual stray magnetic fields and dipolar "flip" interactions between atom pairs in $(n + 2)D_{5/2}$ and $nF_{7/2}$ (see Sec. III A and Ref. [34]) lead to line broadening on the order of 50–100 kHz, which keeps us from reaching the Fourier limit of the linewidth at zero B field in Fig. 4(c). Notably, the three Δm_J-resolved lines at nonzero B field are considerably narrower than the (single) line at B near zero, pointing to dipolar interactions as the main cause for the line broadening at B near zero.

Next, we consider the transition $(n + 2)D_{5/2} \rightarrow nF_{5/2}$. In this case, the g_J factors between the lower and upper levels differ by 0.343, and the five $\Delta m_J = \pm 1$ and six $\Delta m_J = \pm 0$ transitions split by considerably more than in the transition $(n + 2)D_{5/2} \rightarrow nF_{7/2}$, leading to a larger anomaly of the Zeeman effect. Factoring in the distribution of oscillator strength, the overall line pattern features two lines, regardless of microwave polarization, and only the width of the two lines depends on the polarization. The insensitivity of the $(n + 2)D_{5/2} \rightarrow nF_{5/2}$ Zeeman pattern to microwave polarization differs from $(n + 2)D_{5/2} \rightarrow nF_{7/2}$, where the Zeeman pattern strongly depends on microwave polarization. This behavior, which is evident from Figs. 5(b) and 5(c), is a result of the symmetry between line shifts and transition strengths, seen within the $\Delta m_J = 0$ group as well as between the $\Delta m_J = \pm 1$ groups. In addition, for the case of $(n + 2)D_{5/2} \rightarrow nF_{5/2}$ it also is important that π transitions are strongest for large $|m_J|$, while the $\sigma^\pm$ transitions are strongest for small $|m_J|$ [see transition labels in Figs. 5(b) and 5(c)]. Further, the line broadening of the transition $(n + 2)D_{5/2} \rightarrow nF_{5/2}$ near $B = 0$ is considerably less than that of the transition $(n + 2)D_{5/2} \rightarrow nF_{7/2}$. We attribute this difference to the relatively low strength of dipolar "flip" interactions between atom pairs in $(n + 2)D_{5/2}$ and $nF_{5/2}$ (see Sec. III A and Ref. [34]).

For a comprehensive comparison between theory and measurement, we have simulated the Zeeman spectrum using the following principles. (1) Ground-state $|6S_{1/2}, F = 4, m_F\rangle$-populations are m_F independent. (2) Initial Rydberg-state populations $P(F'', m_{F''})$ of the Rydberg states $|(n + 2)D_{5/2}, F'', m_{F''}\rangle$ are computed as described before Eq. (1). This is justified by the small, far-from-saturation Rydberg excitation probabilities in our experiment. (3) Microwave Rydberg-transition probabilities are proportional to $|w_{D_{5/2}, m_J}^{F_J, m_J'}|^2$ [see Eq. (2)]. In Fig. 4 this is justified because microwave powers were chosen well below saturating the Rydberg transitions. (4) All Zeeman Rydberg lines are convoluted with Gaussians of 100 kHz FWHM in order to approximate the observed spectral line broadening of about 140 kHz, which is caused by Rydberg interactions, Zeeman shifts in residual stray magnetic fields, and Stark shifts due to stray electric fields. The Zeeman lines are then summed up to arrive at net spectra $S(\Delta)$. While HFS and FS are included throughout the computation, the HFS of the $(n + 2)D_{5/2}$ Rydberg states

has only marginal effects because it only is in the 10-kHz range, while the HFS of the nF_J Rydberg levels is entirely negligible. The simulated microwave Zeeman spectra are displayed in Figs. 4(e) and 4(f) for the $50D_{5/2} \rightarrow 48F_{7/2}$ and $50D_{5/2} \rightarrow 48F_{5/2}$ transitions, respectively. The simulation reproduces our experimental measurements well, including the two-peak profile for the $50D_{5/2} \rightarrow 48F_{5/2}$ transition and the three-peak profile for the $50D_{5/2} \rightarrow 48F_{7/2}$ transition. For the latter, it was necessary to assume an $\sim 55°$ microwave polarization angle relative to the magnetic-field direction to achieve agreement. Such an angle is quite plausible due to the fact that the microwave is radiated into a complex metal chamber. Comparing measured data and simulated data for a range of polarization angles (not shown), the uncertainty of the polarization angle is determined to be about $\pm 5°$. Further, there is a small shift in the simulation at zero magnetic field and near zero microwave detuning. This shift may be attributed to the HFS of $(n + 2)D_{5/2}$, which is included in the simulation but is otherwise beyond the scope of our present work.

IV. SUMMARY

We have reported the observation of high-resolution microwave spectra of $(n + 2)D_{5/2} \rightarrow nF_J$ transitions in cold cesium atom clouds. For 20-μs-long microwave pulses the observed spectral linewidth was 140 kHz, while for 1-μs pulses coherent, Fourier-limited spectra with pulse areas up to about 3π were achieved, in agreement with a model that takes damping into account. We have further studied the Zeeman effect of the FS-split $(n + 2)D_{5/2} \rightarrow nF_J$ transitions in fields up to about 100 mG. Results agree well with our theoretical

models, which have provided detailed insight into the spectroscopic structure and the microwave electric-field strength and polarization within the atom-field interaction region.

In the future, Rydberg quantum simulators may benefit from our demonstrated coherent drive of relatively strong, high-ℓ transitions. Also, the method allows for microwave field-strength calibration and polarization estimation, which is useful for metal chambers in which computational approaches are prohibitive for field-mode estimation. Furthermore, the work is helpful to null and to calibrate dc magnetic fields in complex vacuum chambers utilizing optical methods and calibration-free atomic spectroscopy. Future simulation work for higher optical and microwave powers will likely require sophisticated methods to solve quantum master equations suitable to treat problems with many quantum states, such as quantum Monte Carlo wave-function simulations (QMCWF; see our previous work in Ref. [23]).

[1] T. F. Gallagher, *Rydberg Atoms*, Cambridge Monographs on Atomic, Molecular and Chemical Physics (Cambridge University Press, Cambridge, 1994).

[2] A. Browaeys and T. Lahaye, Many-body physics with individually-controlled Rydberg atoms, Nat. Phys. **16**, 132 (2020).

[3] Y. Jiao, J. Bai, R. Song, S. Bao, J. Zhao, and S. Jia, Electric field tuned dipolar interaction between Rydberg atoms, Front. Phys. **10**, 892542 (2022).

[4] K. Srakaew, P. Weckesser, S. Hollerith, D. Wei, D. Adler, I. Bloch, and J. Zeiher, A subwavelength atomic array switched by a single Rydberg atom, Nat. Phys. **19**, 714 (2023).

[5] D. Petrosyan and K. Mølmer, Deterministic free-space source of single photons using Rydberg atoms, Phys. Rev. Lett. **121**, 123605 (2018).

[6] S. Shi, B. Xu, K. Zhang, G.-S. Ye, D.-S. Xiang, Y. Liu, J. Wang, D. Su, and L. Li, High-fidelity photonic quantum logic gate based on near-optimal Rydberg single-photon source, Nat. Commun. **13**, 4454 (2022).

[7] A. Padrón-Brito, J. Lowinski, P. Farrera, K. Theophilo, and H. de Riedmatten, Probing the indistinguishability of single photons generated by Rydberg atomic ensembles, Phys. Rev. Res. **3**, 033287 (2021).

[8] D. P. Ornelas-Huerta, A. N. Craddock, E. A. Goldschmidt, A. J. Hachtel, Y. Wang, P. Bienias, A. V. Gorshkov, S. L. Rolston,

and J. V. Porto, On-demand indistinguishable single photons from an efficient and pure source based on a Rydberg ensemble, Optica **7**, 813 (2020).

[9] T. L. Nguyen, J. M. Raimond, C. Sayrin, R. Cortiñas, T. Cantat-Moltrecht, F. Assemat, I. Dotsenko, S. Gleyzes, S. Haroche, G. Roux, T. Jolicoeur, and M. Brune, Towards quantum simulation with circular Rydberg atoms, Phys. Rev. X **8**, 011032 (2018).

[10] D. Jaksch, J. I. Cirac, P. Zoller, S. L. Rolston, R. Côté, and M. D. Lukin, Fast quantum gates for neutral atoms, Phys. Rev. Lett. **85**, 2208 (2000).

[11] E. Urban, T. A. Johnson, T. Henage, L. Isenhower, D. D. Yavuz, T. G. Walker, and M. Saffman, Observation of Rydberg blockade between two atoms, Nat. Phys. **5**, 110 (2009).

[12] M. Jing, Y. Hu, J. Ma, H. Zhang, L. Zhang, L. Xiao, and S. Jia, Atomic superheterodyne receiver based on microwave-dressed Rydberg spectroscopy, Nat. Phys. **16**, 911 (2020).

[13] J. A. Sedlacek, A. Schwettmann, H. Kübler, R. Löw, T. Pfau, and J. P. Shaffer, Microwave electrometry with Rydberg atoms in a vapour cell using bright atomic resonances, Nat. Phys. **8**, 819 (2012).

[14] C. L. Holloway, J. A. Gordon, S. Jefferts, A. Schwarzkopf, D. A. Anderson, S. A. Miller, N. Thaicharoen, and G. Raithel, Broadband Rydberg atom-based electric-field probe for SI-traceable, self-calibrated measurements, IEEE Trans. Antennas Propag. **62**, 6169 (2014).

[15] L. Hao, Y. Xue, J. Fan, J. Bai, Y. Jiao, and J. Zhao, Precise measurement of a weak radio frequency electric field using a resonant atomic probe, Chin. Phys. B **29**, 033201 (2020).

[16] J. Bai, J. Fan, L. Hao, N. L. R. Spong, Y. Jiao, and J. Zhao, Measurement of the near field distribution of a microwave horn using a resonant atomic probe, Applied Sciences **9**, 4895 (2019).

[17] J. A. Gordon, C. L. Holloway, A. Schwarzkopf, D. A. Anderson, S. Miller, N. Thaicharoen, and G. Raithel, Millimeter wave detection via Autler-Townes splitting in rubidium Rydberg atoms, Appl. Phys. Lett. **105**, 024104 (2014).

[18] A. Corney, *Atomic and Laser Spectroscopy* (Oxford University Press, New York, 2006).

[19] D. A. Steck, Cesium D line data, https://steck.us/alkalidata/cesiumnumbers.pdf (2023).

[20] L. Zhang, S. Bao, H. Zhang, G. Raithel, J. Zhao, L. Xiao, and S. Jia, Interplay between optical pumping and Rydberg EIT in magnetic fields, Opt. Express **26**, 29931 (2018).

[21] S. Bao, H. Zhang, J. Zhou, L. Zhang, J. Zhao, L. Xiao, and S. Jia, Polarization spectra of Zeeman sublevels in Rydberg electromagnetically induced transparency, Phys. Rev. A **94**, 043822 (2016).

[22] H. Cheng, H. M. Wang, S. S. Zhang, P. P. Xin, J. Luo, and H. P. Liu, High resolution electromagnetically induced transparency spectroscopy of Rydberg ^{87}Rb atom in a magnetic field, Opt. Express **25**, 33575 (2017).

[23] Y. Xue, L. Hao, Y. Jiao, X. Han, S. Bai, J. Zhao, and G. Raithel, Rydberg electromagnetically induced transparency in a large Hilbert space, Phys. Rev. A **99**, 053426 (2019).

[24] F. Jia, Y. Yu, X. Liu, X. Zhang, L. Zhang, F. Wang, J. Mei, J. Zhang, F. Xie, and Z. Zhong, Dispersive microwave electrometry using Zeeman frequency modulation spectroscopy of electromagnetically induced transparency in Rydberg atoms, Appl. Opt. **59**, 8253 (2020).

[25] F. Jia, J. Zhang, L. Zhang, F. Wang, J. Mei, Y. Yu, Z. Zhong, and F. Xie, Frequency stabilization method for transition to a Rydberg state using Zeeman modulation, Appl. Opt. **59**, 2108 (2020).

[26] L. Ma, D. A. Anderson, and G. Raithel, Paschen-back effects and Rydberg-state diamagnetism in vapor-cell electromagnetically induced transparency, Phys. Rev. A **95**, 061804(R) (2017).

[27] F. Böttcher, A. Gaj, K. M. Westphal, M. Schlagmüller, K. S. Kleinbach, R. Löw, T. C. Liebisch, T. Pfau, and S. Hofferberth, Observation of mixed singlet-triplet Rb$_2$ Rydberg molecules, Phys. Rev. A **93**, 032512 (2016).

[28] S. J. Berl, C. A. Sackett, T. F. Gallagher, and J. Nunkaew, Core polarizability of rubidium using spectroscopy of the *ng* to *nh*, *ni* Rydberg transitions, Phys. Rev. A **102**, 062818 (2020).

[29] J. Lee, J. Nunkaew, and T. F. Gallagher, Microwave spectroscopy of the cold rubidium $(n + 1)d_{5/2} \rightarrow ng$ and *nh* transitions, Phys. Rev. A **94**, 022505 (2016).

[30] K. Moore, A. Duspayev, R. Cardman, and G. Raithel, Measurement of the Rb*g*-series quantum defect using two-photon microwave spectroscopy, Phys. Rev. A **102**, 062817 (2020).

[31] W. Li, I. Mourachko, M. W. Noel, and T. F. Gallagher, Millimeter-wave spectroscopy of cold Rb Rydberg atoms in a magneto-optical trap: Quantum defects of the *ns*, *np*, and *nd* series, Phys. Rev. A **67**, 052502 (2003).

[32] H. Saßmannshausen, F. Merkt, and J. Deiglmayr, High-resolution spectroscopy of Rydberg states in an ultracold cesium gas, Phys. Rev. A **87**, 032519 (2013).

[33] P. Goy, J. M. Raimond, G. Vitrant, and S. Haroche, Millimeter-wave spectroscopy in cesium Rydberg states. quantum defects, fine- and hyperfine-structure measurements, Phys. Rev. A **26**, 2733 (1982).

[34] J. Bai, R. Song, J. Fan, Y. Jiao, J. Zhao, S. Jia, and G. Raithel, Quantum defects of nF_J levels of Cs Rydberg atoms, Phys. Rev. A **108**, 022804 (2023).

[35] R. Cardman and G. Raithel, Hyperfine structure of $nP_{1/2}$ Rydberg states in ^{85}Rb, Phys. Rev. A **106**, 052810 (2022).

[36] C. P. Pearman, C. S. Adams, S. G. Cox, P. F. Griffin, D. A. Smith, and I. G. Hughes, Polarization spectroscopy of a closed atomic transition: Applications to laser frequency locking, J. Phys. B: At., Mol. Opt. Phys. **35**, 5141 (2002).

[37] E. D. Black, An introduction to Pound-Drever-Hall laser frequency stabilization, Am. J. Phys. **69**, 79 (2001).